Power-function expansion of the nondimensional complementary relationship of evaporation: the emergence of dual attractors

Jozsef Szilagyi[a,b,*], Ning Ma[c], Richard D. Crago[d], Russell J. Qualls[e]

[a]Department of Hydraulic and Water Resources Engineering, Budapest University of Technology and Economics, Muegyetem Rkp. 1-3, Budapest, Hungary, H-1111

[b]Conservation and Survey Division, School of Natural Resources, University of Nebraska-Lincoln, 3310 Holdrege St., Lincoln, Nebraska, USA

[c]Key Laboratory of Water Cycle and Related Land Surface Processes, Institute of Geographic Sciences and Natural Resources Research, Chinese Academy of Sciences, Beijing, China

[d]Department of Civil and Environmental Engineering, Bucknell University, Lewisburg, Pennsylvania, USA

[e]Department of Chemical and Biological Engineering, University of Idaho, Moscow, Idaho, USA

[*]Corresponding author, e-mail: szilagyi.jozsef@emk.bme.hu

Key points

i) The power-function extension of the polynomial complementary relationship (CR) of evaporation can account for horizontal moisture advection

ii) Under negligible advection an existing linear version of the nondimensional CR is recaptured

iii) The power-function solution converges to the existing polynomial CR otherwise

Abstract The polynomial form of the nondimensional complementary relationship (CR) follows from an isenthalpic process of evaporation under a constant surface available energy and unchanging wind. The exact polynomial expression results from rationally derived first and second-order boundary conditions (BC). By keeping the BCs, the polynomial can be extended into a two-parameter (a and b) power function for added flexibility. When $a = b = 2$ it reverts to the polynomial version. With the help of Australian FLUXNET data it is demonstrated that the power-function formulation excels among CR-based two-parameter models considered, even when $a = 2$ is prescribed to reduce the number of parameters to calibrate to two. The same power-function approach ($a = 2$) is then employed with a combination of different gridded monthly potential evaporation terms across Australia, while calibrating b against the multiyear simplified water-balance evaporation rate on a cell-by-cell basis. The resulting bi-modal histogram of the b values peaks first near $b = 2$ and then at $b \rightarrow 1$ (secondary modus), confirming earlier findings that occasionally a linear version (i.e., $b = 1$) of the CR yields the best estimates. It is further demonstrated that the linear form emerges when regional-scale transport of moist air is negligible toward the study area during its drying, while the more typical nonlinear CR version prevails otherwise. A thermodynamic-based explanation is yet to be found as to why the flexible power function curves (i.e., $b \neq 2$) converge to the polynomial one ($b = 2$) in such cases.

1. Introduction

The complementary relationship (CR) of evaporation is a powerful tool [see the latest global studies by *Ma et al*. (2021), *Brutsaert et al*. (2020)] for predicting actual land evaporation (E) rates with the help of basic meteorological variables (i.e., air temperature, humidity, net surface radiation and wind speed) all obtained at a single elevation above the ground. Since its original formulation by *Bouchet* (1963), it has evolved into various versions [see *Han & Tian* (2020) for a brief overview] based on different heuristic arguments.

After almost six decades of the groundbreaking study by *Bouchet* (1963), *Szilagyi* (2021) as well as *Crago & Qualls* (2021) gave the CR a stronger physical foundation following the lead of *Monteith* (1981) who first defined the thermodynamic pathway a parcel of air near the evaporating drying surface must follow under unchanging wind conditions and constant available energy (Q_n) at the surface during an adiabatic and isobaric (thus, isenthalpic) process.

Crago & Qualls (2021), *Szilagyi* (2021) extended the study of *Monteith* (1981) by considering a full wet-to-dry cycle and simultaneously tracing the state of the air parcel at the land surface in addition to the one near to it (e.g., 2-m above ground). The key to success lies in the estimation of the wet surface temperature (T_{ws}) from typical drying (i.e., not completely wet) environmental measurements for anchoring the surface isenthalp to the saturation vapor pressure curve in the state diagram.

With the help of the two isenthalps, *Qualls & Crago* (2020) graphically illustrated evaporation from saturated surfaces. Using a similar approach, *Crago & Qualls* (2021) reproduced an existing linear nondimensional formulation of the CR (*Crago & Qualls*, 2018), while *Szilagyi* (2021) independently of them and by a different approach reproduced both the existing linear as well as the nonlinear polynomial formulation of the CR (*Szilagyi et al*., 2017), the latter having been originally inspired by the study of *Brutsaert* (2015).

Here a brief summary of this thermodynamical approach is provided. First the nondimensional linear as well as the polynomial CR equations are derived. Then the latter is expanded by a power function formulation to make it more flexible. The resulting power function with two additional parameters (a and b) is to be applied with daily measurements of air temperature (T), pressure (p), vapor pressure deficit (VPD), net radiation (R_n), ground heat conduction (G) and wind speed (u) in addition to eddy-covariance obtained sensible (H) and latent heat (LE) fluxes for validation at seven Australian FLUXNET sites. The resulting E values are then to be compared with similar estimates of three additional CR-based heuristic evaporation methods by *Kahler & Brutsaert* (2006), *Han & Tian* (2012), and *Gao & Xu* (2021), to demonstrate the predictive capability of the power-function approach. All three methods have two parameters to calibrate, similar to the present power-function one, once one of its parameter values (a) is fixed.

Finally, the power-function approach is to be applied with 0.25-degree spatial resolution gridded monthly input data after aggregation to 0.5-degree values over Australia and its sole free parameter (b) to be calibrated on a cell-by-cell basis against 0.5-degree simplified water-balance derived evaporation estimates (E_{wb}) to see how its value changes spatially and what may drive those changes.

Note that this work is not meant as a calibration/verification analysis of a preferred two-parameter approach over other existing similar (or single parameter) approaches. That is why the steps required for such a study (i.e., validation with data separate from calibration, sensitivity analysis of the parameters, etc.) are deliberately not repeated here, specifically because it would blur the focus of the present work which is the investigation/demonstration, by the help of a recently discovered power-function expansion, of how and when the horizontal advection of humidity over a drying surface produces/affects the thermodynamically-derived linear and nonlinear forms (*Szilagyi*, 2021) of the CR of evaporation and the typical environmental conditions under which, one or the other, emerges.

2. A concise thermodynamical derivation of the nondimensional polynomial complementary relationship

During drying out of the environment under unchanging wind conditions, constant pressure as well as constant available energy, Q_n (= $R_n - G$) at the surface, the change ($d.$) in vapor pressure (e) is strictly tied to changes in air temperature (T) near the surface via the equation

$$de/dT = -\gamma \qquad (1)$$

(*Monteith*, 1981; *Qualls & Crago*, 2020, *Szilagyi*, 2021). Here $\gamma = c_p p(0.622L_v)^{-1}$ is the psychrometric constant, c_p the specific heat of air under constant pressure, and L_v is the latent heat of vaporization. Eq. 1 forms straight (air and surface) isenthalpic lines of slope $-\gamma$ emanating from the saturation vapor pressure curve, $e^*(T)$, in the state diagram of Fig. 1, provided the slight dependence of L_v on T is neglected under typical environmental conditions.

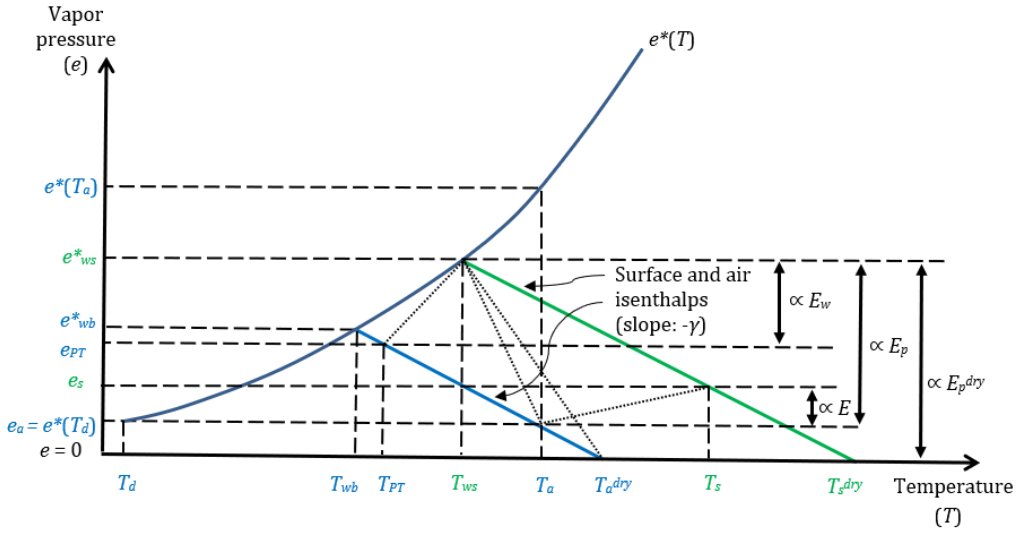

Figure 1. Saturation vapor pressure (e^*) curve, air (blue) and surface (green) isenthalps (*Szilagyi*, 2021; *Crago & Qualls*, 2021) during a full drying-out of the environment from completely wet to a completely dry state. The vertical and horizontal projections of the dotted lines are proportional ($\propto$) to the different latent ($E \le E_w \le E_p \le E_p^{dry}$) and corresponding sensible (the latter negative –directed toward to surface– for E_p and E_p^{dry}) heat fluxes. See Table 1 for definition of the different variables.

The saturation vapor pressure (hPa) can be obtained, e.g., by the Teten's formula as $e^*(T) = 6.108\exp[17.27T / (237.3 + T)]$ where T is supplied in C° (*Stull*, 2000). The wet-bulb temperature, T_{wb}, is the lowest temperature the air at the measurement height can attain by evaporation, but this temperature is rarely reached during natural processes due to large-scale vertical mixing of free tropospheric air into the boundary layer (*Brutsaert*, 1982). Instead, a wet environment air temperature, $T_{PT} \geq T_{wb}$, generally occurs. T_{PT} however is not known during drying conditions of the environment (i.e., when $T_a > T_{PT}$), but it can be estimated by the wet-surface temperature, T_{ws}, because in humid conditions air temperature changes mildly with elevation above the ground (*Laikhtman*,1964; *Stull*, 2000; *Szilagyi*, 2014).

T_{ws} can be estimated (*Szilagyi & Jozsa*, 2008) by writing out the Bowen ratio (i.e., H / LE) for a small wet patch utilizing the *Penman* (1948) equation for E_p (mm d^{-1}), yielding the evaporation rate of such a small wet area, as

$$\frac{H}{LE} = \frac{Q_n - E_p}{E_p} \approx \gamma \frac{T_{ws} - T_a}{e^*(T_{ws}) - e_a} \tag{2}$$

where the small size of the wet patch means it cannot alter the temperature and humidity of the overpassing air significantly, measured upwind of it. Note that E specified in water depth can be transformed into energy flux (LE) values by $LE = L_v \rho_w E$, and vice-versa for Q_n, where ρ_w is the density of water. Eq. 2 is implicit for T_{ws}, requiring iterations to solve. The Penman equation is given by

$$E_p = \frac{\Delta Q_n}{\Delta + \gamma} + \frac{\gamma f_u [e^*(T_a) - e_a]}{\Delta + \gamma} \tag{3}$$

where Δ denotes the slope of the saturation vapor pressure curve (hPa C°$^{-1}$) at the measured air temperature T_a, and the empirical wind function, f_u (mm d^{-1} hPa^{-1}), is traditionally specified as $f_u = 0.26(1 + 0.54u_2)$ (*Brutsaert*, 1982). Here u_2 (m s^{-1}) is the horizontal wind speed at 2-m above the ground and can be estimated by a power function (*Brutsaert*, 1982) from measurements (u_h) at h meters above the surface as $u_2 = u_h (2 / h)^{1/7}$. The $e^*(T_a) - e_a$ expression in the aerodynamic term of Eq. 3 is often referred to as the vapor pressure deficit (*VPD*).

With the two isenthalps anchored to the saturation vapor pressure curve, one may notice that during a full wet-to-dry transition of the environment the (T_a, e_a) state-coordinate points traverse the (T_{PT} - T_a^{dry}, e_{PT} - 0), while the corresponding state-coordinates (T_s, e_s) track the full length of the (T_{ws} - T_s^{dry}, e^*_{ws} - 0) distance on the surface isenthalp. From the two different distances travelled during the same amount of time, two different average speed values result for the movement of the respective state coordinates. By assuming that the ratio of distances travelled on the two isenthalps during any time interval equals the constant ratio of the two average speed values, a geometric similarity emerges (*Szilagyi*, 2021; c.f. *Crago & Qualls*, 2021, who used somewhat different reasoning), namely

$$\frac{e_a}{e_{PT}} = \frac{e_s}{e^*_{ws}} \tag{4}$$

which can be augmented into

$$\frac{e_a}{e_{PT}} = \frac{e^*_{ws}-(e^*_{ws}-e_a)}{e^*_{ws}-(e^*_{ws}-e_{PT})} = \frac{e_s}{e^*_{ws}} \quad (5)$$

The right-hand-side of Eq. 4 can be further expanded into

$$\frac{e_s}{e^*_{ws}} = \frac{e_s(1-\frac{e_a}{e_s})}{e^*_{ws}(1-\frac{e_a}{e_s})} = \frac{e_s(1-\frac{e_{PT}}{e^*_{ws}})}{e^*_{ws}(1-\frac{e_{PT}}{e^*_{ws}})} = \frac{e_s-\frac{e_s}{e^*_{ws}}e_{PT}}{e^*_{ws}-e_{PT}} = \frac{e_s-e_a}{e^*_{ws}-e_{PT}} \quad (6)$$

The combination of Eqs. 5 and 6 yields (*Szilagyi*, 2021)

$$\frac{e_s-e_a}{e^*_{ws}-e_{PT}} = \frac{e^*_{ws}-(e^*_{ws}-e_a)}{e^*_{ws}-(e^*_{ws}-e_{PT})} \quad (7)$$

which via the corresponding evaporation terms in Fig. 1 can be written as

$$\frac{E}{E_w} = \frac{E_p^{dry}-E_p}{E_p^{dry}-E_w} \quad (8)$$

due to the Dalton-type formulation of any evaporation term as $E = -K\, de/dz = K_z\,(e_s - e_a)$ where K is the turbulent diffusion coefficient, z is vertical distance and K_z is K divided by the measurement height.

In Eq. 8, E_p^{dry} can be obtained by Eq. 3 with the $e_a = 0$ substitution, and e^* and Δ evaluated at the dry-environment air temperature, T_{dry} ($= T_a + e_a / \gamma$) (*Szilagyi*, 2021). The wet-environment evaporation rate, E_w, can be obtained from the *Priestley-Taylor* (1972) equation as

$$E_w = \alpha \frac{\Delta(T_{PT})Q_n}{\Delta(T_{PT})+\gamma} \quad (9)$$

The unknown wet-environment air temperature, T_{PT}, can be substituted by the lesser of T_{ws} and T_a because T_{PT} can never exceed T_a due to the cooling effect of evaporation, while T_{ws} can during high relative-humidity conditions (*Szilagyi*, 2014, 2021). The spatially and temporally constant value of the Priestley-Taylor (PT) coefficient, α, can be set without any calibration with gridded data, covering a large spatial domain and thus ensuring the presence of permanently or periodically wet areas, by the method of *Szilagyi et al*. (2017), otherwise, it must be calibrated, typically within the [1 – 1.32] interval (*Morton*, 1983).

Eq. 8 can be rearranged after dividing it by E_p (*Szilagyi et al.*, 2017; *Crago & Qualls*, 2018) into

$$y = X; \quad y := \frac{E}{E_p},\ X := w_i \frac{E_w}{E_p},\ w_i := \frac{E_p^{dry}-E_p}{E_p^{dry}-E_w} \quad (10)$$

which is a linear relationship between the two nondimensional variables y and X. Notice that w_i acts as a wetness index, with $w_i \approx 0$ for hyper arid and $w_i = 1$ for wet conditions (*Szilagyi et al*., 2017). Note also that the two nondimensional variables were already obtained by *Szilagyi et al*. (2017) in a different way, before the present thermodynamic-based derivation was found. The complementarity in the CR means that E and E_p change in opposite ways (*Bouchet*, 1963), best seen in Eq. 10 between E and E_pX. When E_p increases (i.e., the environment dries), w_i decreases while E_w remains unchanged, yielding a decreased E rate.

As an area dries, large-scale horizontal advection of more humid air from the surrounding larger region may occur. This is especially true for areas lying downwind from a sea, or other large body of water, or areas surrounded by mountains having much wetter conditions. This influx of external humid air suppresses or completely eliminates the weak vertical humidity gradient that would otherwise exist. This means that the resulting suppressed and therefore vanishing $e_s - e_a$ term in Eq. 7 would not respond anymore to changes in e_s and therefore to the ensuing e_a that a change in e_s would normally generate, leaving the left-hand-side of Eq. 7 unresponsive to any changes in (the transported) e_a itself, thus causing $dy / dX \rightarrow 0$ when $X \rightarrow 0$ (*Szilagyi*, 2021). Note that e^*_{ws} and e_{PT} are conservative (invariant) quantities only under isenthalpic processes and any humidity advection violates this adiabatic requirement but the resulting changes in e^*_{ws} and e_{PT} are treated negligible in this study (as in *Szilagyi*, 2021) which is probably acceptable as long as the humidity transport itself is not too excessive.

With consideration of the four boundary conditions (BC) of i) $y = 1 \mid X = 1$; ii) $dy / dX = 1 \mid X = 1$, iii) $y = 0 \mid X = 0$; iv) $dy / dX = 0 \mid X = 0$ and seeking a polynomial solution, the following nondimensional complementary relationship

$$y = 2X^2 - X^3 \tag{11}$$

is obtained (*Szilagyi et al.*, 2017; *Szilagyi*, 2021). Note also that when the horizontal advection of humidity is negligible then the last BC is absent, yielding the linear form, Eq. 10, of the CR. Figure 2 depicts the two solutions.

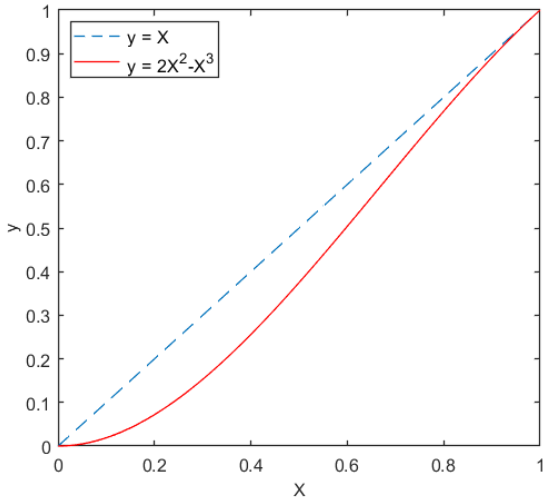

Figure 2. The linear and nonlinear polynomial CR relationships between $y = E\,E_p^{-1}$ and $X = w_i\,E_w\,E_p^{-1}$.

Eq. 11 has already been applied on a monthly basis in a calibration-free mode, employing a spatially and temporally constant PT-α value with great success (outperforming mainstream complex, data-intensive evaporation models) over the US (*Szilagyi et al.*, 2017; *Kim et al.*, 2019; *Ma & Szilagyi*, 2019; *Ma et al.*, 2020), China (*Ma et al.*, 2019), and the globe (*Ma et al.*, 2021). It is distinct from a similar model formulation of *Liu et al.* (2018), and *Brutsaert et al.* (2020) in two important aspects. Firstly, in the evaluation of Δ within the PT-equation the latter sources

ignore the temperature change between actual (i.e., drying) and wet environmental conditions. Secondly, and more importantly, in their nondimensional variable, x, playing the role of X here, the wetness index, w_i, does not appear as their derivation of x is heuristic, not based on thermodynamics. As a result, their $x = E_w E_p^{-1}$ value can only approach zero when the available energy at the surface, Q_n, does so in E_w, since E_p is bounded. In order to broaden the resulting limited range of the x values the PT-α value must be lowered significantly with growing aridity, much below its physically meaningful lower-bound value of unity. Their treatment of the PT-α simply as a tunable parameter thus negates the original purpose of the PT-equation, which is to account for the entraintment of free tropospheric air into the boundary layer (*Lhomme*, 1997) strictly under wet environmental conditions. See *Szilagyi et al*. (2020) for an in-depth discussion of this issue.

Table 1. List of the different evaporation (E) rates employed in the study together with the relevant temperature (T) and vapor pressure (e) terms defined.

E, LE	Actual evaporation, latent-heat rate
E_p	Potential (Penman) evaporation rate
E_p^{dry}	Dry-environment potential evaporation rate
E_w	Wet-environment (Priestley-Taylor) evaporation rate
T_a, e_a [$= e^*(T_d)$]	Actual air temperature, vapor pressure
T_a^{dry}	Dry-environment air temperature
T_d	Dew-point temperature
T_{PT}, e_{PT}	Wet-environment air temperature, vapor pressure
T_{wb}, e^*_{wb}	Wet-bulb temperature, vapor pressure
T_s, e_s	Actual land-surface temperature, vapor pressure
T_s^{dry}	Dry-environment land surface temperature
T_{ws}, e^*_{ws}	Wet surface temperature (*Szilagyi and Jozsa*, 2008), vapor pressure

3. Expansion of the polynomial complementary relationship by a power function approach

The polynomial in Eq. 11 can be expanded by a power-function approach using the same BCs. The resulting function

$$y = aX^b - (a-1)X^{\frac{ab-1}{a-1}} \qquad a, b > 1 \tag{12}$$

has two parameters additional to Eq. 11, a and b. Fig. 3 displays the ensuing curves for selected values of a and b. With the value of b increasing (from 1.4 to 2 to 3) the curves move to the right, forming three groups of curves with the a and b values picked for demonstration. Within each group the curves move upward with increasing values of a. For example, the lowest (i.e., right-most) curve has $a = 1.1$ and $b = 3$, while the one just above it belongs to $a = 1.2$, $b = 3$. For most practical applications the parameter ranges can be narrowed to $1 < a \leq 2$ and $1 < b < 10$.

In order to reduce the number of parameters to just two (the PT-α, and b) in Eq. 12 for a meaningful comparison with other existing two-parameter CR-based methods, $a = 2$ is prescribed in this study for evaporation estimation. It makes also possible that the power-function curve revert to the polynomial of Eq. 11 during calibration when necessary. Fig. 4

displays the curves with a prescribed value $a = 2$, and $1 < b \leq 10$. The curve with $a = 2$ and $b = 1.001$ indeed has a vanishing slope at $X = 0$, as BC iv) requires, but it is indistinguishable from the $y = X$ line of Eq. 10 by the naked eye. For this reason, during calibration of b in the ensuing analysis with $a = 2$ imposed, a value of $b = 1$ will be allowed for practicality, even though it violates BC iv).

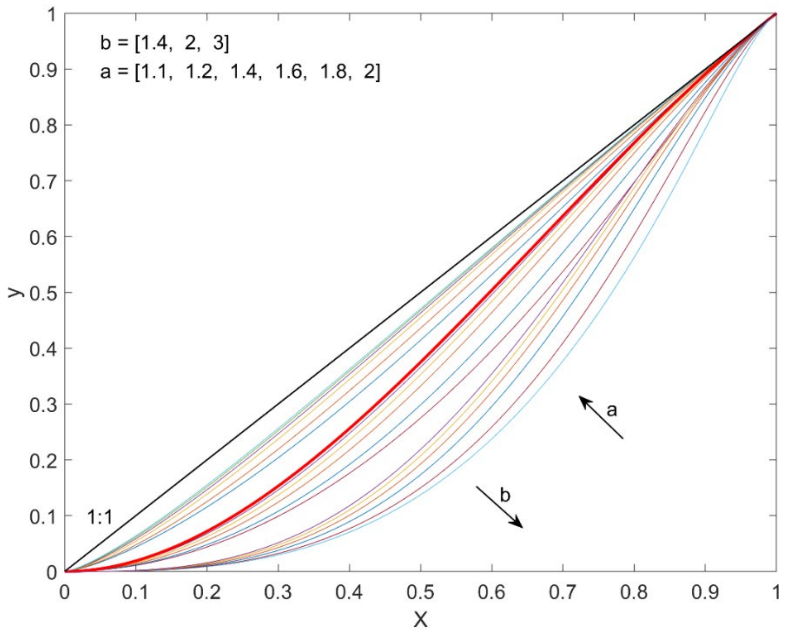

Figure 3. Graphical representation of Eq. 12 for selected values of a and b. The polynomial of Eq. 11 ($a = b = 2$) is the heavier red line.

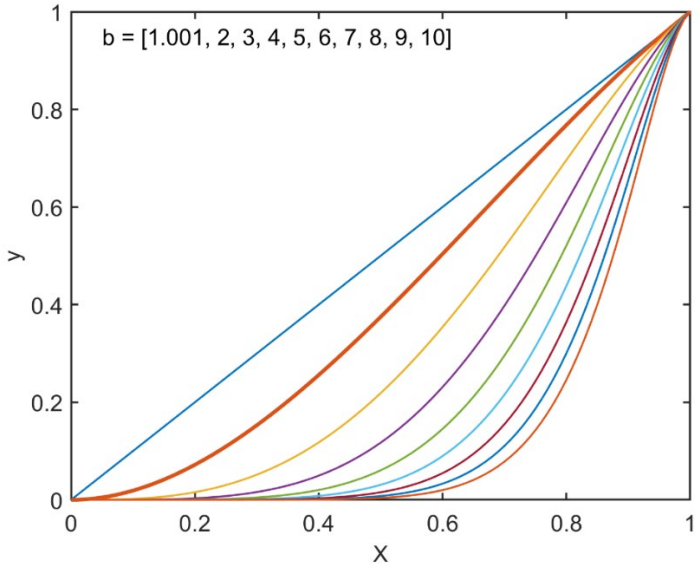

Figure 4. Graphical representation of Eq. 12 for $a = 2$ and $1 < b \leq 10$. The polynomial of Eq. 11 ($a = b = 2$) is the heavier red line.

4. Testing the power-function approach with eddy-covariance data

The polynomial (Eq. 11) as well as the power-function (Eq. 12) formulations of the CR are tested with eddy-covariance data of seven Australian FLUXNET sites, diplayed in Fig. 5. These sites include land covers of grass, permanent wetland, open shrubland, woody savanna, and evergreen broadleaf forests. See Table 1 in *Crago & Qualls* (2018) for more information on the measurements, and Table 4 below for geographic coordinates and periods of record. In the ensuing modeling measurement heights for wind speed are reduced by the average height of the vegetation. The daily eddy-covariance-measured LE fluxes are Bowen-ratio corrected [i.e., $LE_c = Q_n\,(1+H\,LE^{-1})$] to close the energy budget (*Twine et al*., 2000), and the temperature values converted to potential temperatures, $T_p = T_a + gz_m\,/\,c_p$, where z_m is the measurement height for air temperature, and g is the gravitational acceleration (e.g., *Stull*, 2000) due to the relatively large scatter in z_m among the sites (from 2.5 m for grass to 70 m for the forests). Note that in theory, T_p must replace T_a in the preceding equations (as sensible heat fluxes are driven by vertical gradients of T_p and not T_a), but the difference between them is negligible for measurement heights not far from the ground in comparison to the observed vertical change in T_a.

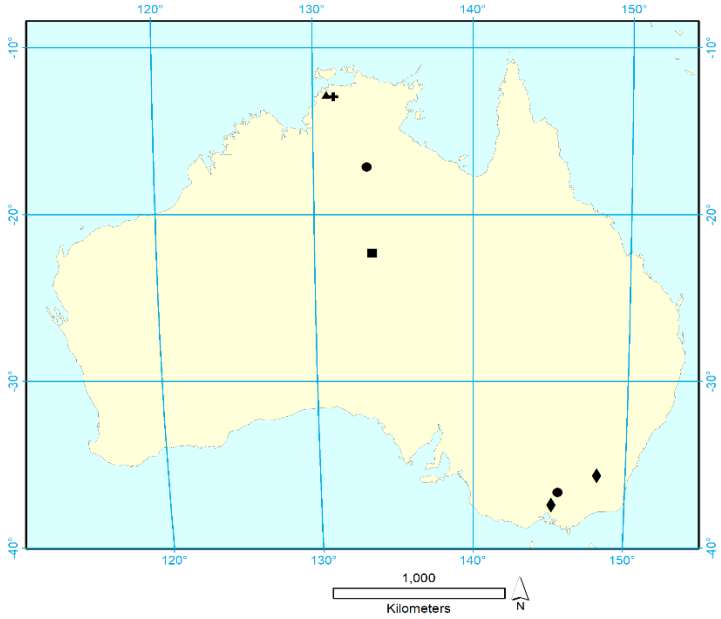

Figure 5. Location of the seven FLUXNET sites (see Table 4 for exact coordinates) with at least one year of daily meteorological and eddy-covariance derived flux measurements. ✚: permanent wetland; ▲: woody savanna; ■: open shrubland; ●: grassland; ♦: evergreen broadleaf forest.

The evaporation estimates of Eqs. 11 and 12, employing daily, 5- and 30-day aggregated input data are compared to similar estimates of three additional two-parameter heuristic CR-based models by *Kahler & Brutsaert* (2006), *Han & Tian* (2012), and *Gao & Xu* (2021), to be referred to as KB06, HT12 and GX21, respectively. In all three models and in Eq. 12, the two tunable parameters include the PT-α and an additional parameter (Table 2) for a meaningful comparison

of the CR models. The exact representation of HT12 is chosen specifically for such a purpose of a shared PT-α.

Table 2 summarizes the three models. KB06 and HT12 evaluate Eq. 9 at the drying air temperature, T_a, while GX21 adopts the approach of *Szilagyi & Jozsa* (2008) for estimating T_{ws} and thus T_{PT} (*Szilagyi*, 2014). For additional information of the models, please, refer to the relevant publication.

Table 2. Summary of the three additional two-parameter CR-based models employed in this study.

KB06	HT12*	GX21
$y = (1 + c^{-1})\, x - c^{-1}$ $x_{KB} = E_w(T_a)\, E_p^{-1}$ Parameters: α, c	$y = [1 + k\,(x^{-1} - 1)^n]^{-1}$ $x_{HT} = \alpha^{-1}\, E_w(T_a)\, E_p^{-1}$ $x_h = (0.5 + c_{HT}^{-1})[\alpha(1 + c_{HT}^{-1})]^{-1}$ $n = 4\alpha(1 + c_{HT}^{-1})\, x_h\,(1 - x_h)$ $k = [x_h\,(1 - x_h)^{-1}]^n$ Parameters: α, c_{HT}	$y = \exp[(1 - x^{-d})d^{-1}]$ $x = E_w\, E_p^{-1}$ Parameters: α, d

*Written in the form specified in *Han & Tian* (2018).

A 5-day aggregation instead of a weekly one is chosen, because *Morton* (1983) argues that it is the shortest time-interval over which any effect of passing weather systems, temporarily upsetting the dynamic equilibrium between the surface and the overlying air, can be expected to be substantially subdued.

Performance of the calibrated models is summarized in Table 3. The four (plus Eq. 11) models behave similarly in terms of the root-mean-square error (RMSE), but Eq. 12 produces the best results in seven out of the nine cases considered, followed by Eq. 11 (four occasions, provided Eq. 12 is excluded) and KB06 (twice). In fact, Eq. 12 is always the best performing model with 30-day aggregated data. In KB06 the calibrated values of the PT-α occasionally drop below the physically meaningful unity value while it is almost the norm for GX21. Interestingly, the best-fit-line slope deviates from its optimal value of unity the least with Eq. 11.

Fig. 6 demonstrates the increasing effect of large-scale horizontal moisture transport on the shape of the nondimensional CR curve of Eq. 12, as aridity progresses. For the evergreen broadleaved forests serious aridity never occurs as the majority of the points are situated at $X > 0.5$ (Fig. 6b), with corresponding evaporation rates, $E_{EC} > 1$ mm d^{-1} (Fig. 6a), therefore the effect of any possible horizontal moisture transport toward these sites remains negligible. As a result, calibration of Eq. 12 yields $b \rightarrow 1$ and thus the straight line of Eq. 10 (red line in Fig. 6b, on top of the 1:1 line). More serious aridity, on the other hand, can develop over the grass sites resulting in several points at $X < 0.2$ (Fig. 6d), and $E_{EC} < 0.5$ mm d^{-1} (Fig. 6c). Any horizontal moisture transport to the grass sites somewhat drier than their environs will leave the eddy-covariance measurements largely unaffected in the beginning of drying when vertical gradients of the vapor pressure over the grass are still significant, but nonetheless, will depress the value of E_p (which is

very sensitive to moisture changes in its *VPD* term due to the steep slope of the saturation vapor pressure curve at high temperatures), and thus boost the wetness index, w_i, within X, which then moves the measurement points to the right horizontally in Fig. 6d, away from the 1:1 line for $0.2 < X < 0.45$. The measurement points however will follow the diminishing slope of Eq. 12 at extreme low X (< 0.2) values (as seen in Fig. 6d) and get closer to the 1:1 line again when large-scale horizontal moisture advection itself weakens as arid conditions probably spread spatially.

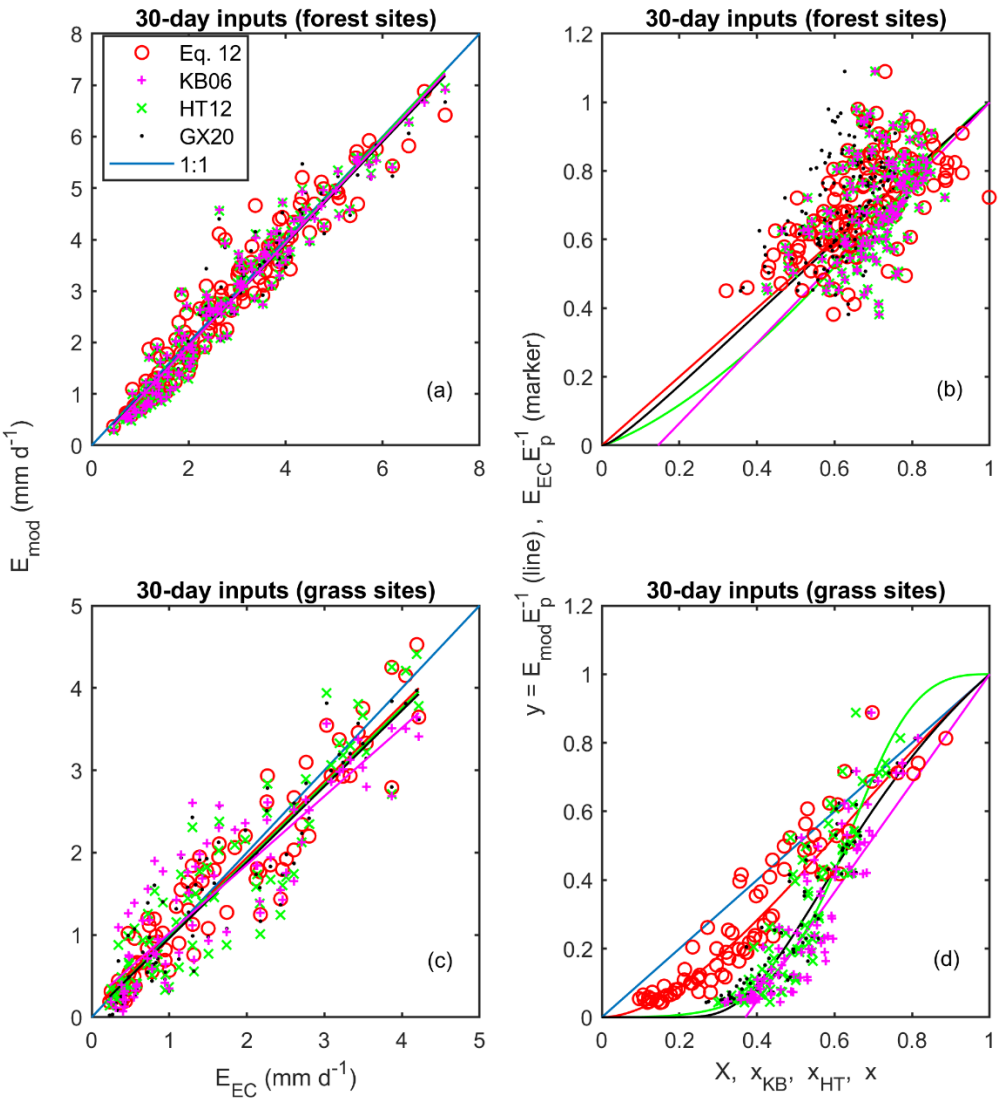

Figure 6. Regression plots of the modeled (E_{mod}) 30-day evaporation rates against eddy-covariance measurements (E_{EC}) at two forested (a) and two grass (c) sites of FLUXNET in Australia (see Fig. 5 for locations) together with the least-squares-fitted straight lines. Graphical representation of the calibrated (see Table 3) nondimensional formulas (b, d) listed in Table 2 plus that of Eq. 12, displayed with the nondimensional E_{EC} measurements. Color coding for the best-fit lines and the theoretical curves comes from the markers.

Note that the 1:1 line forms a theoretical upper limit to the measured nondimensional evaporation rates for KB06 and GX21 only, as these models relate $E\ E_p^{-1}$ to $E_w\ E_p^{-1}$ with the $E \leq E_w$ expectation. While such is the case mostly for the grass sites (Fig. 6d), it is not so for the forested ones (Fig. 6b), due to their incorrect scaling that produces x_{KB} and x (Table 2), respectively, instead of the thermodynamically backed one for X, first suggested by *Szilagyi et al*. (2017).

Table 3. Root-mean-square error (RMSE) values (in mm d^{-1} for easier comparison among aggregation periods) of the CR-based two-, and single-parameter (Eq. 11) evaporation estimation methods at different Australian FLUXNET sites displayed in Fig. 5. The trial-and-error-calibrated parameter values of the different methods are also displayed, together with the resulting slope (m) of the best-fit line. The lowest RMSE values among the two-parameter methods are displayed in bold for each aggregation period and group of sites considered. The single-parameter estimate (Eq. 11) is bold-faced when it yields better estimates than the two-parameter methods (without Eq. 12).

Station/aggregation	Eq. 12	Eq. 11	KB06	HT12	GX21
All (seven sites) Daily	**0.81** a=1.11, b=1.3 m=0.83	0.89 α=1.16 m=0.94	0.84 α=1.04, c=1.95 m=0.84	0.84 α=1.09, c_{HT}=1.3 m=0.86	0.86 α=0.93, d=1.07 m=0.85
5-day	**0.66** α=1.13, b=1.45 m=0.87	0.72 α=1.17 m=0.96	0.71 α=1.08, c=1.6 m=0.9	0.7 α=1.13, c_{HT}=1.1 m=0.91	0.71 α=0.97, d=1.35 m=0.9
30-day	**0.51** α=1.14, b=1.55 m=0.91	**0.56** α=1.17 m=1	0.58 α=1.1, c=1.5 m=0.95	0.59 α=1.14, c_{HT}=1.1 m=0.94	0.59 α=0.98, d=1.38 m=0.93
Grass (two sites) Daily	**0.7** α=1.12, b=1.65 m=0.75	**0.72** α=1.18 m=0.83	0.83 α=0.96, c=2.25 m=0.66	.75 α=1.15, c_{HT}=0.9 m=0.75	0.75 α=0.96, d=1.46 m=0.74
5-day	**0.55** α=1.16, b=1.75 m=0.83	**0.57** α=1.21 m=0.9	0.69 α=1.02, c=1.85 m=0.75	0.61 α=1.18, c_{HT}=0.9 m=0.81	0.6 α=1.02, d=1.73 m=0.84
30-day	**0.37** α=1.21, b=1.85 m=0.93	**0.38** α=1.24 m=0.98	0.55 α=1.06, c=1.7 m=0.83	0.48 α=1.24, c_{HT}=0.8 m=0.93	0.46 α=1.05, d=1.81 m=0.92
Forest (two sites) Daily	0.75 α=1.11, b=1 m=0.93	0.92 α=1.15 m=0.98	**0.65** α=0.94, c=46.4 m=0.96	0.67 α=1, c_{HT}=5 m=1	0.7 α=0.86, d=0.1 m=0.96
5-day	0.55 α=1.12, b=1 m=0.94	0.66 α=1.16 m=1	**0.52** α=0.98, c=7.64 m=0.98	0.53 α=1, c_{HT}=4.4 m=1	0.55 α=0.88, d=0.1 m=0.98
30-day	**0.4** α=1.13, b=1 m=0.98	0.48 α=1.17 m=1.06	0.42 α=1, c=5.9 m=1	0.41 α=1, c_{HT}=5 m=1.01	0.43 α=0.89, d=0.1 m=0.99

Testing the power-function approach with gridded simplified water-balance data

Eq. 12 is further tested across Australia for the spatial distribution of its b value, employing 0.25-degree monthly estimates of E_w, E_p and E_p^{dry} calculated with data from sources specified in the global study of *Ma et al*. (2021), except that R_n now comes from the Global Land Data Assimilation System Version 2.1 (*Beaudoing & Rodell*, 2020). The above monthly evaporation

terms are aggregated to 0.5-degree spatial resolution over the 2003-2012 time period together with the 0.25-degree precipitation values from the Global Precipitation Climatology Center (GPCC) Full Data Monthly Version 2018 (*Schneider et al*., 2018). Multi-year, simplified water-balance derived evaporation (E_{wb}) rates as precipitation less runoff are calculated on a cell-by-cell basis by taking the arithmetic mean of two monthly 0.5-degree gridded global runoff rates from the gauge-derived database of *Ghiggi et al*. (2019), and the synthesis of eleven land surface models by *Hobeichi et al*. (2019). The two sources of the runoff values are necessary due to the scarcity and uneven distribution of the monitoring watersheds (*Fowler et al*., 2021) across Australia large enough to accommodate the model cells. As only the multi-year mean annual E_{wb} values are needed for the present purpose of investigating the spatial distribution of b in Eq. 12, any possible changes in annual cell-water storage can be assumed to exert a negligible influence on the multiyear E_{wb} value (*Brutsaert*, 1982) and especially on the spatial distribution characteristics of b.

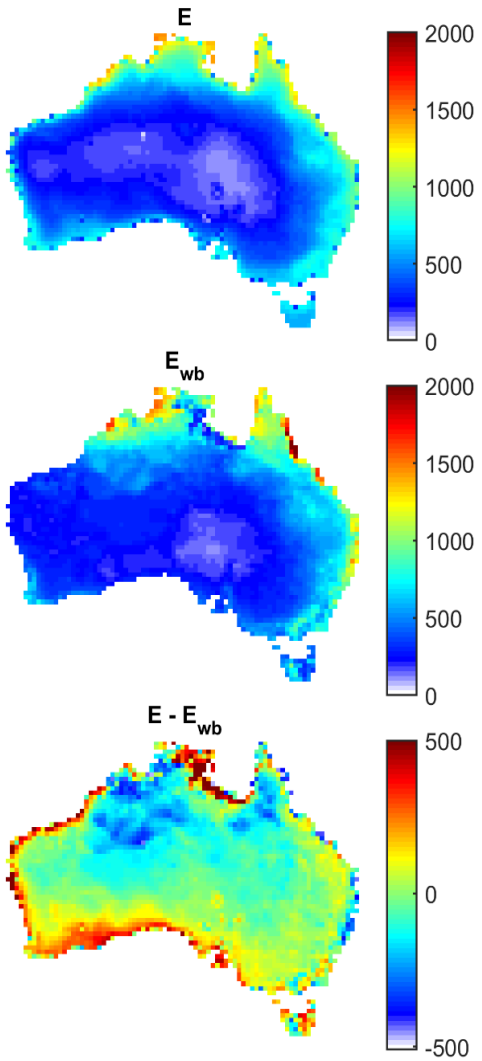

Figure 7. Spatial distribution of the 0.5-degree multiyear (2003-2012) mean annual evaporation rates (mm a^{-1}) across Australia by a) Eq. 11; b) simplified water balance (E_{wb}), and; c) their difference.

The polynomial equation (Eq. 11) without any calibration, estimates (Fig. 7) the continent-wide (with Tasmania included) multiyear mean annual water-balance evaporation (E_{wb}) rate of 462 mm a^{-1} within 4% (E = 447 mm a^{-1}). The value of the PT-α in Eq. 11 was set to 1.1 globally by *Ma et al*. (2021) via the method of *Szilagyi et al*. (2017), requiring no calibration, therefore no precipitation or runoff data. (Note that such a calibration-free setting of the PT-α value can only be performed for large-scale data sets ensuring the presence of permanently or at least periodically wet areas within their spatial domain.)

The polynomial CR (Eq. 11) overestimates the water-balance evaporation rates near the southern and western seashore where the prevailing winds carry moisture laden air from the ocean to the land, thus decoupling its moisture content from that of the underlying arid or semi-arid land surface. Naturally, the more arid the land is, the stronger this overestimation. The strongest overestimation, however, occurs along the western side of the Gulf of Carpentaria in the north where the E_{wb} values are unusually low along a south-west to north-east patch, for reasons not known to these authors. Otherwise, Eq. 11 generally underestimates the water-balance values in northern Australia characterized by a monsoonal precipitation regime, for reasons discussed below.

The value of the parameter b in Eq. 12 (a = 2, α = 1.1) is calibrated on a cell-by-cell basis by minimizing the absolute difference in the multi-year mean annual model-estimated and water-balance derived evaporation rates. Fig. 8a displays the resulting spatial distribution of the calibrated values. As seen, the spatial pattern of the values strongly follows that of the estimation error in Fig. 7: elevated values where the estimation error is positive and depressed ones where it is negative. This is to be expected, as the measurement points (E_{wb} or E_{EC}) are fixed in the nondimensional graph once the value of α is set within X. An overestimation (i.e., when the curve is above a given marker point in e.g., Fig. 6d) in Eq. 12 can only be corrected by moving the curve to the right which is achieved by increasing the value of b (Fig. 4), and vice versa for an underestimation.

Naturally, the calibration yields model estimates very close to the 'observed' values (Fig. 8b, c, d) in each cell with only a low number of exceptions. The multiyear mean annual value though remains practically the same (E = 448 mm a^{-1}) as before, suggesting that the b = 2 value implicit in Eq. 11 and therefore Eq. 11 itself with its rational boundary conditions, is physically well founded and indeed obeyed by nature, at least, in a statistical sense. The histogram of the calibrated values of b (Fig. 9) with an ensemble mean of 2.08 and a median value of 1.9, further corroborates this finding.

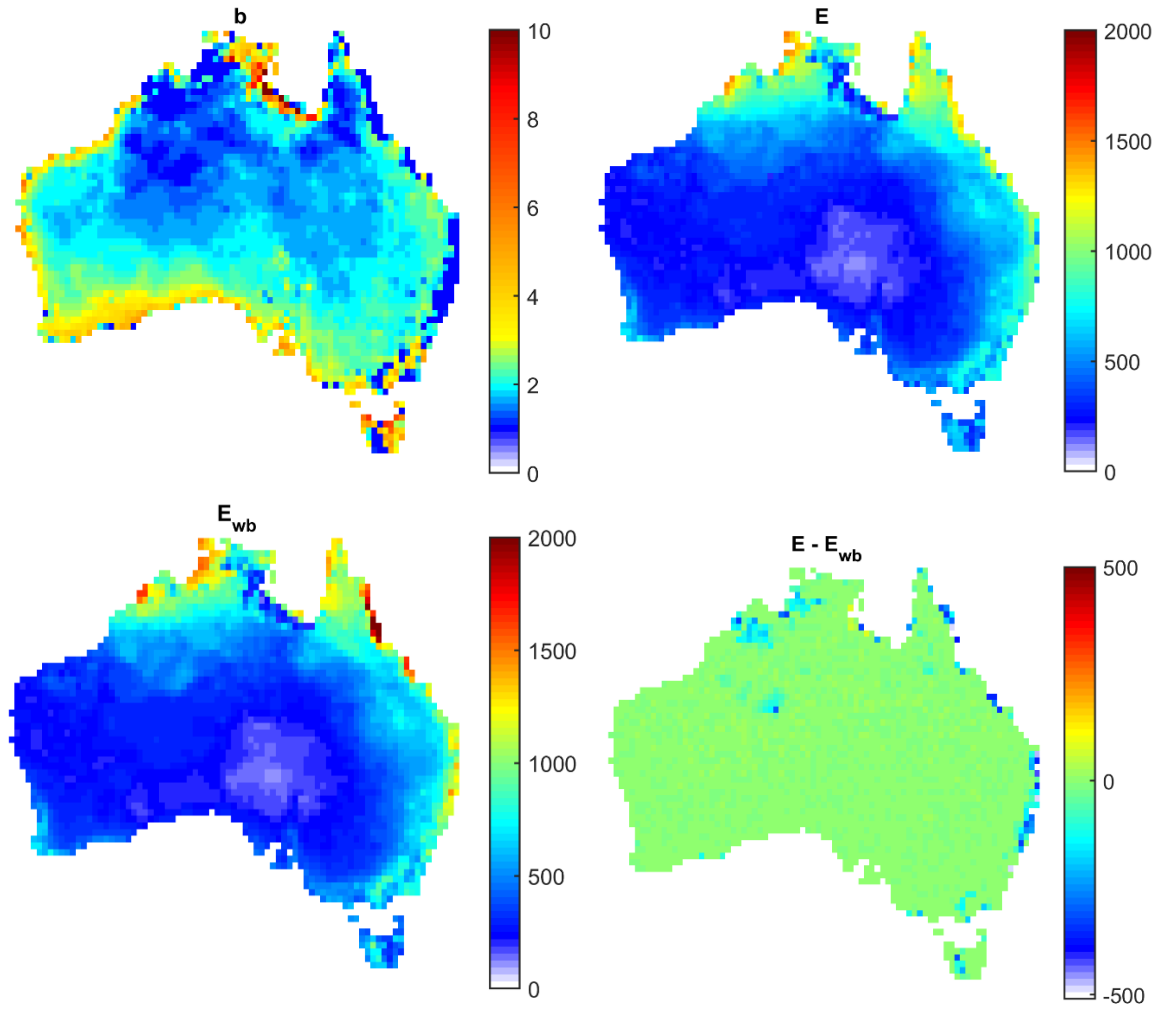

Figure 8. Spatial distribution of the a) calibrated value of b in Eq. 12; b) resulting multi-year (2003-2012) mean annual evaporation rates (mm a^{-1}) by Eq. 12 (E); c) simplified water-balance (E_{wb}) estimates for comparison, and; d) their difference.

An interesting property of the histogram is that it is bimodal, with a secondary peak near $b = 1$. As discussed above, a unity value of b and a linear relationship between y and X (except in the vicinity of $X = 0$ where the slope must vanish due to the BCs in Eqs. 11 and 12) result in theory when in Fig. 1 the relative speed of the state coordinates along the isenthalps stays constant during drying out of the environment (until hyper arid conditions are reached near $X = 0$). Such conditions however may most commonly exist while the environment remains relatively humid as seen at the forest sites, and thus, the effect of any possible large-scale horizontal moisture transport toward the drying area continues to be negligible. Indeed, this must be the case along almost the entire eastern coast of Australia, the north-western part of the Northern Territory, the eastern side of the Gulf of Carpentaria, within the Australian Alps as well as the western part of Tasmania, all where annual precipitation rates are the highest and aridity the lowest (Fig. 10), forcing the calibrated values of b to remain unity (Fig. 8a).

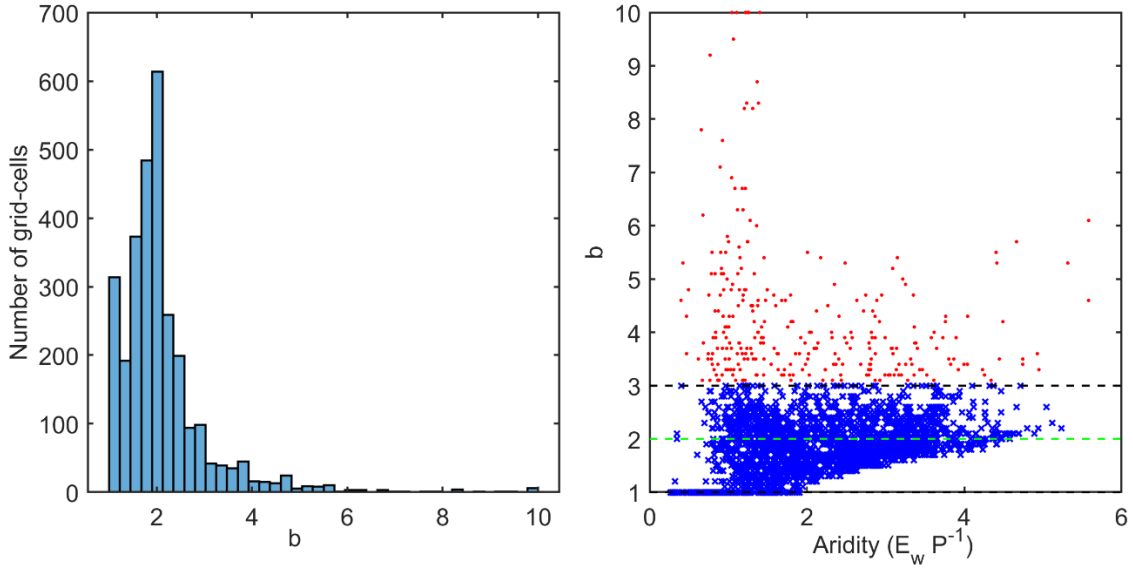

Figure 9. a) Histogram of the b values obtained via a cell-by-cell calibration of Eq. 12 against the multiyear mean annual E_{wb} rate. b) The calibrated b values plotted against the aridity index (ratio of the wet-environment evaporation rate, E_w, and precipitation), marked by red dots when $b > 3$.

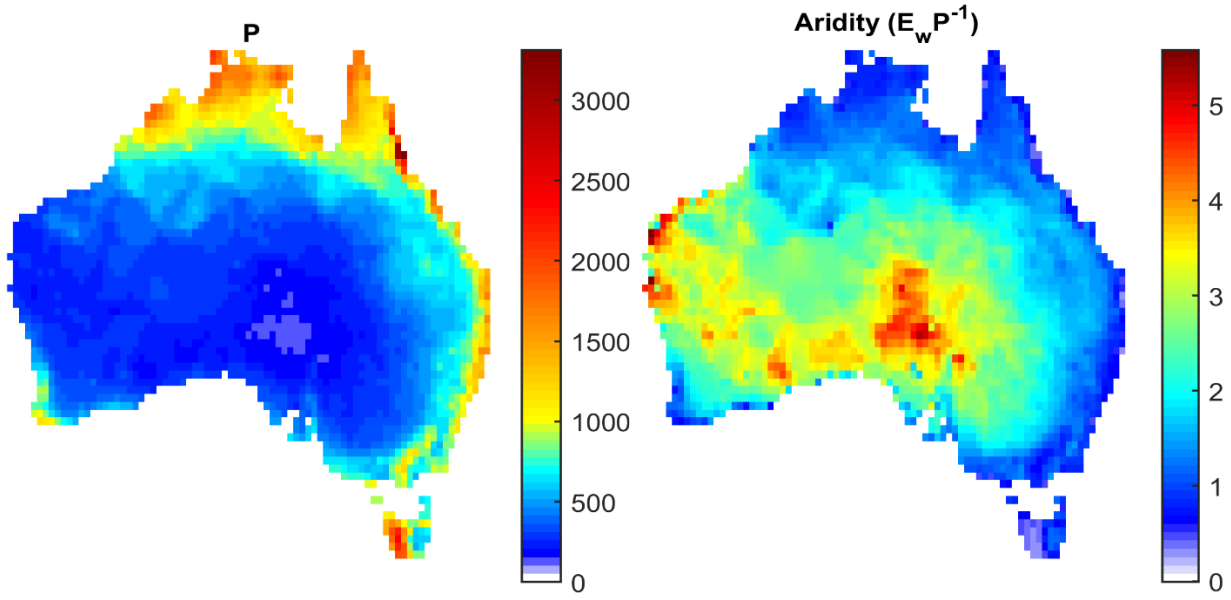

Figure 10. Spatial distribution of the multi-year (2003-2012) mean annual precipitation (P) rates (mm a^{-1}) and the aridity index (ratio of the wet-environment evaporation rate, E_w, and P).

As seen in Fig. 9, about 95% of the histogram values are less than three. In fact, $b > 3$ occurs predominantly along the dry southern and western seashore (Fig. 8a) as a result of an overestimation of Eq. 11 (Fig. 7) due to the significant moisture transport from the ocean decoupling the moisture status of the air from its land surface. (A similar overestimation by Eq. 11 along the western side of the Gulf of Carpentaria is most likely the consequence of the underestimated water-balance-derived values in Fig. 8c). The calibrated $b < 3$ values, assumed to

represent the required coupled state (with only minimal advection) of the air and the underlying land surface, scatter around the value of two in Fig. 9b but with a decreasing range and an increasing lower envelope as aridity grows. When the aridity index is less than about unity, signifying wet environmental conditions, the predominant value of b becomes unity, as discussed above. The scatter in the b values of Fig. 9b makes it hard to predict the value of b based on some index of environmental aridity, except when the environment is either very humid ($b \rightarrow 1$) or increasingly arid ($b \rightarrow 2$). This is not surprising, as the value of b generally depends on the strength of the horizontal moisture advection which in turn is influenced by the existing moisture difference between the study area and its larger, regional environment. This dynamic interplay explains the underestimation of Eq. 11 in the monsoonal northern part of Australia, where in the wet phase of the monsoon the $b = 2$ value implicit in Eq. 11 (instead of the calibrated b values close to unity seen in Fig. 8a) underestimates the wet evaporation rates while in the dry phase of the monsoon with its lower land evaporation rates it cannot make up for it, even when the $b = 2$ value then is probably correct.

The consistency in the spatial distribution of the calibrated b values is perhaps most striking when one compares the gridded-data-derived values with those obtained from the FLUXNET measurements, both listed in Table 4. Only at the southernmost site is there a significant difference in the two calibrated values, where the large-scale horizontal moisture transport from the nearby (about 70 km away) ocean is felt by the grid cell covering not only the forest but other land-covers (*ESA*, 2009) expected to be drier than the forested land (Fig. 11).

Table 4. Calibrated values of b in Eq. 12 from the FLUXNET 30-day aggregated measurements and the monthly gridded data of *Ma et al*. (2021) for the grid-cell (2003-2012) covering the site.

FLUXNET sites in Fig. 5 (from north to south) with period of records displayed	FLUXNET site latitude, longitude (decimal degrees)	FLUXNET b	Grid-cell b
Woody savanna (2001-2014)	12.5S, 131.15E	1	1
Permanent wetland (2006-2008)	12.54S, 131.31E	1	1
Grassland (North) (2008-2014)	17.15S, 133.35E	1.7	1.6
Open shrubland (2013)	22.29S, 133.64E	2	1.9
Evergreen broadleaf forest (East) (2001-2014)	35.66S, 148.15E	1	1
Grassland (South) (2012-2014)	36.65S, 145.58E	1.9	2.3
Evergreen broadleaf forest (West) (2005-2008)	37.43S, 145.19E	1	1.9

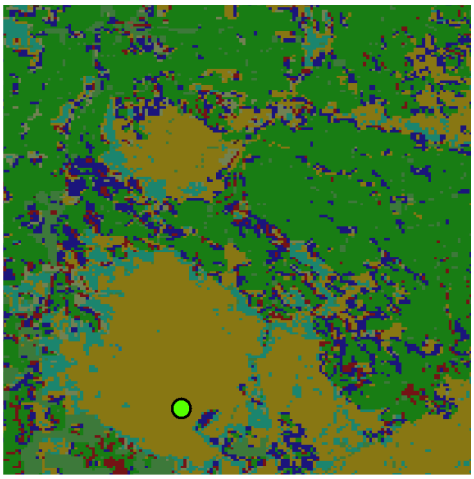

Figure 11. Location (circle) of the evergreen broadleaf forest (West) FLUXNET site of Table 4 (last row) within the 0.5-degree grid-cell covering it. The predominant land-cover category according to the United Nations Land Cover Classification System (LCCS) is 'rainfed croplands' in green color (*ESA*, 2009). The forested areas are displayed in brown. The cell is about 55 km in size.

Table 4 also indicates that the value of b and its spatial behavior with gridded data are not influenced or constrained by a correctly set constant value (i.e., $\alpha = 1.1$) of the PT-α since with FLUXNET data both PT-α and b are simultaneously calibrated yet yield practically the same value of b as the gridded data. A systematic increase in the correctly set constant value of the PT-α for the gridded data –in order to bring it closer to the average PT-α value of 1.14 with the 30-day aggregated FLUXNET data– results in growing differences in the two calibrated values of b at the FLUXNET sites (not shown). But this is again to be expected, as *Szilagyi et al*. (2017) pointed out that the optimal value of the PT-α is influenced by the spatial and temporal resolution of the input data itself.

5. Summary and conclusions

The power-function extension, Eq. 12, of the nondimensional polynomial CR of Eq. 11, the latter derived from thermodynamic considerations, introduces two parameters, a and b, additional to the PT-α in Eq. 11. By setting $a = 2$, Eq. 12 can reproduce Eq. 11 via the $b = 2$ choice, and the linear CR of Eq. 10, provided $b = 1$.

Calibration of the PT-α and b with FLUXNET data (while $a = 2$) results in a two-parameter CR version that excels among three additional heuristic two-parameter CR models in its estimation of the daily, 5- and 30-day aggregated latent heat fluxes. The calibrated value of b becomes unity with 30-day aggregated inputs at four FLUXNET sites, two of them situated in a wet climate with mean annual precipitation in excess of 1500 mm, while the other two sites are located in broadleaved forests enjoying about 700 mm of rain annually. At the driest, open shrubland, site the calibrated value of b becomes 2, while at the remaining two sites somewhat smaller than that.

With the help of gridded precipitation and runoff data the calibration of b is repeated on a cell-by-cell basis with 0.5-degree gridded monthly inputs to Eq. 12 across Australia over a whole

458 decade with a spatially and temporally constant PT-α value of 1.1, set by the method of *Szilagyi*
459 *et al*. (2017). The FLUXNET-derived b values are almost perfectly recaptured for the cells that
460 cover the FLUXNET sites. Only at one forest site is there a larger difference where the
461 predominant land cover of the 0.5-degree cell overlying the site is rainfed cropland which
462 probably explains the difference in the calibrated b values, i.e., unity for the forested site and 1.9
463 for the cell.

464 The grid-calibrated b values follow a bimodal distribution with a primary mode around two
465 (mean of 2.08 and median of 1.9) and a secondary one near unity. It helps explain earlier
466 findings by *Crago & Qualls* (2018) for the same FLUXNET sites, plus the current site-by-site
467 FLUXNET calibration results of why a linear nondimensional CR relationship (corresponding to
468 $a = 2$, $b = 1$ in Eq. 12) yields the best estimate for certain locations.

469 While *Szilagyi* (2021) in his thermodynamics-based derivation of Eq. 11 correctly deduced that a
470 a vanishing slope of the corresponding curve near $X = 0$ can only occur when the difference in e_s
471 and e_a also vanishes, he failed to identify the process that can produce it in general. The spatial
472 distribution of the calibrated b values in Fig. 8, plus the site-by-site calibration results, help
473 finding it. That process is the horizontal, regional transport of humidity toward the drying area
474 which can clearly produce a vertically near constant humidity gradient and thus a vanishing
475 difference in the e_s and e_a values near $X = 0$. This horizontal humidity transport then sets the
476 second-order BC at $X = 0$ to $dy / dX = 0$ and thus produces Eq. 11. Further exploration is required
477 to explain why this polynomial solution acts as an attractor to the more flexible power-function
478 expansion (yielding a mean b value of 2.08 and a median of 1.9), considering that the polynomial
479 (just like the power-function) approach is just a mathematical convenience (satisfying the four
480 BCs) without any physically based differential equation behind it. The linear solution of Eq. 10
481 as the other attractor for the power-function curves, in contrast, results from purely
482 thermodynamic reasoning.

483 When the effect of the horizontal transport of humidity is negligible due to minimal spatial
484 differences in moisture during slight-to-moderate drying of the study region, typically in
485 permanently or at least periodically humid (due to monsoonal rains) environments, the constant
486 relative speed conjecture of the state coordinates, (e, T) vs (e_s, T_s) along the air and surface
487 isenthalps (Fig. 1), first postulated by *Szilagyi* (2021), seems to be validated by the calibrated b
488 values of unity, and thus reproducing (except near $X = 0$) the linear CR version of Eq. 10.
489 Naturally, the preservation of a constant relative speed between the two isenthalps' state
490 coordinates cannot be expected to exist in a strict sense, at all times, due to unavoidable changes
491 in Q_n, air pressure, and/or wind conditions during the averaging period (typically from day to
492 month), but rather in a statistical sense, as a mean behavior over the averaging period.

493 Eq. 12 may be preferrable over the existing single-parameter (and calibration-free when applied
494 with gridded data of a large domain) polynomial approach of Eq. 11, due to its built-in flexibility
495 when calibration is made possible by available measured (e.g., eddy-covariance derived) or
496 water-balance based E estimates and/or the possibility exists that a linear CR approach (i.e.,
497 when $a = 2$ and $b = 1$ in Eq. 12) yields (even temporarily, during wet conditions that appear in
498 monsoonal regions) a better estimate than Eq. 11.

Data availability All data used in this study are publicly available from the following sites. Daily FLUXNET values (http://fluxnet.fluxdata.org/sites/site-list-and-pages/); GPCC precipitation (https://opendata.dwd.de/climate_environment/GPCC/html/fulldata-monthly_v2018_doi_download.html); runoff data (https://doi.org/10.6084/m9.figshare.9228176, https://geonetwork.nci.org.au/geonetwork/srv/eng/catalog.search#/metadata/f9617_9854_8096_5291); ERA5 and ERA5-Land data (https://www.ecmwf.int/en/forecasts/datasets/reanalysis-datasets/era5); R_n (https://disc.gsfc.nasa.gov/datasets/GLDAS_NOAH025_M_2.1/summary).

Acknowledgment Support provided by the Ministry of Innovation and Technology of Hungary from the National Research, Development and Innovation Fund, financed under the TKP2021 funding scheme (project# BME-NVA-02), and by USDA NIFA grant IDA01584 is kindly acknowledged.

References

Beaudoing, H., & Rodell, M. (2020). GLDAS Noah Land Surface Model L4 monthly 0.25 × 0.25 degree V2.1. Greenbelt, Maryland, USA Goddard Earth Sciences Data and Information Services Center (GES DISC). https://doi.org/10.5067/SXAVCZFAQLNO

Bouchet, R. (1963). Evapotranspiration reelle et potentielle, signification climatique. *International Association of Hydrological Sciences Publication*, *62*, 134-142.

Brutsaert, W. (1982). *Evaporation into the atmosphere: Theory, history, and applications*, Dordrecht. Holland: D. Reidel. https://doi.org/10.1007/978-94-017-1497-6

Brutsaert, W. (2015). A generalized complementary principle with physical constraints for land-surface evaporation. *Water Resources Research*, *51*(10), 8087-8093. https://doi.org/10.1002/2015WR017720

Brutsaert, W., Cheng, L., & Zhang, L. (2020). Spatial distribution of global landscape evaporation in the early twenty-first century by means of a generalized complementary approach. *Journal of Hydrometeorology*, *21*, 287-298. https://doi.org/10.1175/JHM-D-19-480 0208.1

Crago, R., & Qualls, R. (2018). Evaluation of the Generalized and rescaled complementary relationships. *Water Resources Research*, *54*, 8086-8102. https://doi.org/10.1029/2018WR023401

Crago R., & Qualls, R. (2021). A graphical interpretation of the rescaled complementary relationship for evapotranspiration. *Water Resources Research*, *57*(8). https://doi.org/10.1029/2020WR028299

European Space Agency (ESA) (2009). GlobCover 2009. Last accessed January 15, 2022 at https://databasin.org/datasets/a08ff893bed248d2b6add102a3aa0101/

Fowler, K. J. A., Acharya, S. C., Addor, N., Chou, C., & Peel, M. C. (2021). CAMELS-AUS: hydrometeorological time series and landscape attributes for 222 catchments in Australia. *Earth System Science Data*, 13, 3847-3867. https://doi.org/10.5194/essd-570 13-3847-2021

Gao, B., & Xu, X. (2020). Derivation of an exponential complementary function with physical constraints for land surface evaporation estimation. *Journal of Hydrology*, *593*. https://doi.org/10.1016/j.jhydrol.2020.125623

Ghiggi, G., Humphrey, V., Seneviratne, S. I., & Gudmundsson, L. (2019). GRUN: an observations-based global gridded runoff dataset from 1902 to 2014. *Earth System Science Data*, *11*, 1655-1674. https://doi.org/10.5194/essd-11-1655-2019

Han, S., Hu, H., & Tian, F. (2012). A nonlinear function approach for the normalized complementary relationship evaporation model. *Hydrological Processes*, *26*(26), 3973-3981. https://doi.org/10.1002/hyp.8414

Han, S., & Tian, F. (2018). Derivation of a sigmoid generalized complementary function for evaporation with physical constraints. *Water Resources Research*, *54*, 5050-5068. https://doi.org/10.1029/2017WR021755

Han, S., & Tian, F. (2020). A review of the complementary principle of evaporation: From original linear relationship to generalized nonlinear functions. *Hydrology and Earth System Sciences*, *24*, 2269-2285. https://doi.org/ 10.5194/hess-2019-545

Hobeichi, S., Abramowitz, G., Evans, J., & Beck, H. E. (2019). Linear Optimal Runoff Aggregate (LORA): a global gridded synthesis runoff product. *Hydrology and Earth System Sciences*, *23*, 851-870. https://doi.org/10.5194/hess-23-851-2019

Kahler, D. M., & Brutsaert, W. (2006). Complementary relationship between daily evaporation in the environment and pan evaporation. *Water Resources Research*, *42*, W05413. https://doi.org/10.1029/02005WR004541

Kim, D., Lee, W.-S., Kim, S. T., & Chun, J. A. (2019). Historical drought assessment over the contiguous United States using the generalized complementary principle of evapotranspiration. *Water Resources Research*, *55*. https://doi.org/10.1029/2019WR024991

Laikhtman, D. L. (1964). Physics of the Boundary Layer of the Atmosphere, Sivan Press, Israel.

Lhomme, J. P. (1997). A theoretical basis for the Priestley-Taylor coefficient. *Boundary-Layer Meteorology, 82*(2), 179-191. https://doi.org/10.1023/A:1000281114105

Liu, X., Liu, C., & Brutsaert, W. (2018). Investigation of a generalized nonlinear form of the complementary principle for evaporation estimation. *Journal of Geophysical Research: Atmospheres*, *123*(8), 3933-3942. https://doi.org/10.1002/2017JD028035

Ma, N., & Szilagyi, J. (2019). The CR of evaporation: a calibration-free diagnostic and benchmarking tool for large-scale terrestrial evapotranspiration modeling. *Water Resources Research*, *55*. https://doi.org/10.1029/2019WR024867

570 Ma, N., Szilagyi, J., Zhang, Y., & Liu, W. (2019). Complementary-relationship-based modeling
571 of terrestrial evapotranspiration across China during 1982-2012: Validations and spatiotemporal
572 analyses. *Journal of Geophysical Research-Atmospheres*, 124. https://doi.org/2018JD029850

573 Ma, N., Szilagyi, J., & Zhang, Y. (2021). Calibration-free complementary relationship estimates
574 terrestrial evapotranspiration globally. *Water Resources Researc*h, *57*, e2021WR029691.
575 https://doi.org/10.1029/2021WR029691

576 Monteith, J. L. (1981). Evaporation and surface temperature: Evaporation and surface
577 temperature. *Quarterly Journal of the Royal Meteorological Society*, *107*(451), 1-27.
578 https://doi.org/10.1002/qj.49710745102

579 Morton, F. I. (1983). Operational estimates of areal evapotranspiration and their significance to
580 the science and practice of hydrology. *Journal of Hydrology, 66*, 1-76.

581 Penman, H. L. (1948). Natural evaporation from open water, bare soil and grass. *Proceedings of*
582 *the Royal Society A: Mathematics, Physics and Engineering Sciences, 193*, 120-145.
583 https://doi.org/10.1098/rspa.1948.0037

584 Priestley, C. H. B., & Taylor, R. J. (1972). On the assessment of surface heat flux and
585 evaporation using large-scale parameters. *Monthly Weather Rev*iew, *100*(2), 81-92.

586 Qualls, R. J., & Crago, R. D. (2020). Graphical interpretation of wet surface evaporation
587 equations. *Water Resources Research*, *56*, e2019WR026766.
588 https://doi.org/10.1029/2019WR026766

589 Schneider, U., Becker, A., Finger, P., Meyer-Christoffer, A., & Ziese, M. (2018). GPCC Full
590 data monthly product version 2018 at 0.25°: Monthly land-surface precipitation from rain-gauges
591 built on GTS-based and historical data.
592 https://doi.org/10.5676/DWD_GPCC/FD_M_V2018_025

593 Stull, R. B. (2000). Meteorology for Scientists and Engineers. Brooks/Cole, Pacific Grove, CA,
594 USA.

595 Szilagyi, J. (2014). Temperature corrections in the Priestley-Taylor equation of evaporation.
596 *Journal of Hydrology*, 519, 455-464. https://doi.org/10.1016/j.jhydrol.2014.07.040

597 Szilagyi, J. (2018). A calibration-free, robust estimation of monthly land surface
598 evapotranspiration rates for continental-scale hydrology. *Hydrology Research*, *49*.
599 https://doi.org/10.2166/nh.2017.078

600 Szilagyi, J. (2021). On the thermodynamic foundations of the complementary relationship of
601 evaporation. *Journal of Hydrology*, *593*, 125916. https://doi.org/10.1016/j.jhydrol.2020.125916

602 Szilagyi, J., & Jozsa, J. (2008). New findings about the Complementary Relationship-based
603 evaporation estimation methods. *Journal of Hydrology*, *354*, 171-186.
604 https://doi.org/10.1016/j.jhydrol.2008.03.008

Szilagyi, J., Crago, R., & Qualls, R. (2017). A calibration-free formulation of the complementary relationship of evaporation for continental-scale hydrology. *Journal of Geophysical Research-Atmospheres*, *122*, 264-278. https://doi.org/10.1002/2016JD025611

Szilagyi, J., Crago, R., & Ma, N. (2020). Dynamic scaling of the generalized complementary relationship (GCR) improves long-term tendency estimates in land evaporation. *Advances in Atmospheric Sciences*, *37* (9), 1–12. https://doi.org/10.1007/s00376-020-0079-6

Twine, T. E., Kustas, W. P., Norman, J. M., Cook, D. R., Houser, P. R., Meyers, T. P., Prueger, J. H., Starks, P. J., & Wesely, M. L. (2000). Correcting eddy-covariance flux underestimates over a grassland. *Agricultural and Forest Meteorology*, *103*(3), 279-300. https://doi.org/10.1016/S0168-1923(00)00123-4